Temperature dependences of Cr^{+3} radiative and nonradiative transitions in ruby and emerald

W. H. Fonger and C. W. Struck
RCA Laboratories, Princeton, New Jersey 08540
(Received 16 December 1974)

The sequence of Cr^{+3} temperature effects in ruby and emerald deduced by Kisliuk and Moore is analyzed quantitatively by the quantum-mechanical single-configurational-coordinate model. The energy parabolas are positioned so that the thermal Franck-Condon weights account both for the positions and shapes of the optical bands and, through the nonradiative rates, for the thermal quenchings of emissions. Parabola phonon energies near 500 cm^{-1} explain the overall optical-band shapes disregarding fine structure, and larger phonon energies near 800 cm^{-1} explain the nonradiative rates. Relative to the small-offset parabolas, the large-offset $^4T_2$ and $^4T_1$ parabolas have to be downshifted by a few kT units with increasing temperature to take into account effects of lattice thermal expansion. The $^4T_2$ downshift enhances $^4T_2$ thermal repopulation from ^2E. In the single-ion model used, quantum losses occur only above 450 °K due to thermally activated $^2E \rightarrow {}^4T_2 \rightarrow {}^4A_2$ processes, and the $^4T_2 \rightarrow {}^4A_2$ transitions occur at energies closer to the $^4T_2$ parabola minimum than to the $^4T_2$, $^4A_2$ crossover. Forster's sequence of ruby temperature effects and the different quantum efficiencies reported for excitation into ^2E and $^4T_2$ are not possible in the model.

I. INTRODUCTION

We have recently given a unified treatment[1] of the temperature quenching of narrow-line and broad-band emissions using the quantum-mechanical single-configurational-coordinate (QMSCC) model. The most interesting applications are to centers such as Cr^{+3} or Eu^{+3} with several intersecting electronic states, and Cr^{+3} in ruby and emerald is treated here. This case is excellent because the Franck-Condon (FC) offset is intermediate—large enough for FC effects yet small enough for accurate parabola placements through observed zero-phonon energies.

The single-configurational-coordinate (SCC) diagram explaining ruby spectra is shown in Fig. 1. This diagram admits narrow absorption lines to the smaller-offset states ^2E, $^2T_1$, and $^2T_2$ near 14 400, 15 000, and 21 000 cm^{-1} and broad absorption bands to the larger-offset states $^4T_2$ and $^4T_1$ near 18 000 and 25 000 cm^{-1}. These absorption transitions may be seen in McClure's Cr^{+3} paper[2] or review.[3] In emission, the diagram admits a narrow $^2E \rightarrow {}^4A_2$ line near 14 400 cm^{-1} plus, at higher temperatures where $^2T_1$ and $^4T_2$ are populated thermally from ^2E, a narrow $^2T_1 \rightarrow {}^4A_2$ line and a broad $^4T_2 \rightarrow {}^4A_2$ band, both near 15 000 cm^{-1}.

The work here builds on earlier studies by Misu[4] and Kisliuk and Moore[5] (KM). Misu was the first to use a SCC diagram for ruby and to recognize the broad-band emission occurring at higher temperatures as the FC-shifted counterpart of the absorption band to $^4T_2$.

Misu's detailed SCC diagram and sequence of ruby temperature effects were arranged to give different quantum efficiencies for excitation into ^2E and $^4T_2$ and also to accommodate nonradiative transitions described by Mott's crossover rate $A_M \exp(-E_X/kT)$.[1,6] As discussed below, these particular features should not be incorporated into a ruby SCC model.

KM extended Misu's work and also applied it to emerald. The $^2E \rightarrow {}^4T_2$ energy is smaller in emerald than in ruby, and, by comparing the temperatures of corresponding effects in the two materials, KM developed the sequence of temperature effects accepted here as correct. Excitation into any state relaxes rapidly and efficiently to ^2E and gives efficient $^2E \rightarrow {}^4A_2$ line emission. With increasing temperature, a $^4T_2$ population builds up thermally from ^2E, and $^2E \rightarrow {}^4A_2$ line emission is progressively replaced by the faster $^4T_2 \rightarrow {}^4A_2$ broad-band emission (above 350 °K in ruby, above 100 °K in emerald) and by $^4T_2 \rightarrow {}^4A_2$ nonradiative losses (above 450 °K in both materials). For the nonradiative transitions, KM ignored their SCC diagram and used Kiel's multiphonon-emission rate[7] $A_K \epsilon^p (1+\langle m \rangle_v)^p$. Kiel's rate is inaccurate for the large-offset $^4T_2 \rightarrow {}^4A_2$ transition,[1] and KM's analysis is superceded by the quantitative analysis here.

Forster[8] reviewed the ruby work and, because of certain discrepancies, disallowed KM's sequence of temperature effects and developed a different sequence. The discrepancies are discussed below. Forster's model is excluded.

II. RUBY OPTICAL BANDS

A. SCC model by the matrix method

We use the QMSCC model in the thermal-Condon approximation and handled by the U, V-matrix method.[1] The radiative rates are constant; the

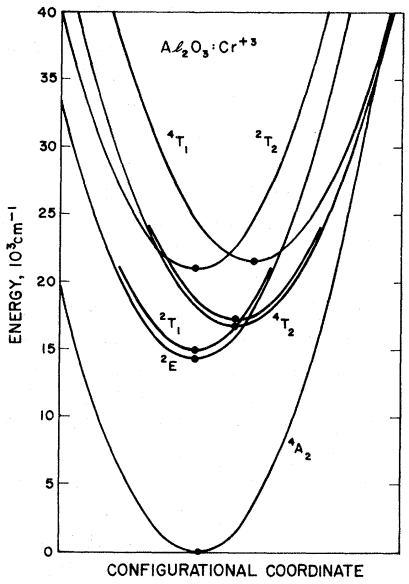

FIG. 1. SCC diagram of the Cr^{+3} states in ruby.

nonradiative rates increase with temperature. For $u \rightleftarrows v$ transitions, the temperature-dependent optical band shapes and nonradiative rates are given by summed thermal-FC weights U_{p_U}, V_{p_V} in Eq. (8) of Ref. 1. The FC factors are obtained through the Manneback recursion formulas[9] plus an averaging procedure. The U_{p_U} (V_{p_V}) distribution for p_U (p_V) = 0, ±1, ±2, ··· gives the normalized $v \rightarrow u$ ($u \rightarrow v$) optical band at energies $p_U \hbar\omega_u$ ($p_V \hbar\omega_v$) from the zero-phonon energy $h\nu_{zp,vu}$; $\hbar\omega_u$, $\hbar\omega_v$ are the parabola phonon energies. For the particular p_U (p_V) indices in Eq. (10) of Ref. 1 giving $h\nu_{zp,vu}$ in units of $\hbar\omega_u$ ($\hbar\omega_v$), $N_{uv}U_{p_U}$ ($N_{vu}V_{p_V}$) gives the $v \rightarrow u$ ($u \rightarrow v$) nonradiative rate, where N_{uv} (N_{vu}) is an electronic factor near 10^{13} sec^{-1}.

The parabola placements and other model parameters are chosen empirically to give an overall fit to optical-band shapes and to nonradiative rates as determined from thermal quenchings of emissions. Both types of data are used in the fitting because the model's predictions for both depend sensitively on the parameters.

B. Offset $^4A_2 \rightleftarrows {}^4T_2, {}^4T_1$ transitions

For $^4A_2(u) \rightleftarrows {}^4T_2(v)$ transitions, the parameter values are Manneback angle $\theta = 44°$, offset parameter $a_{uv} = 3.526$, $\hbar\omega_v = 500$ cm^{-1}, and $h\nu_{zp,vu} = 16\,770$ $cm^{-1} - 1.4\,kT$. These values in turn fix $\hbar\omega_u = 536$ cm^{-1} and the Huang-Rhys-Pekar factors $S_v = 3$, $S_u = 3.217$; see Ref. 1. The choice $\theta = 44°$ makes the $^4T_2$ parabola flatter than the $^4A_2$ parabola so that the absorption band is closer to $h\nu_{zp,vu}$. The first moments are $S_v\hbar\omega_v = 1500$ cm^{-1} in absorption, $S_u\hbar\omega_u = 1725$ cm^{-1} in emission.[10]

The absorption band differs somewhat in σ and π polarizations.[2,3] Thus, two $^4T_2$ parabolas are shown in Fig. 1. The zero-phonon energy cited above describes the lower σ parabola. The model fit to Brossel and Margerie's[11] 2 °K σ absorption band is shown in Fig. 2, the curve with points being the measured band. The zero-phonon line at 16 770 cm^{-1} (596 nm) and adjacent peaks at multiples of 200 cm^{-1} showing 200-cm^{-1} phonons[12] are evident. The curve labeled 500 cm^{-1} gives the model fit. The 200 and 833 cm^{-1} curves show alternative fits with θ and $h\nu_{zp,vu}$ fixed but a_{uv}, $\hbar\omega_u$, $\hbar\omega_v$, S_u, S_v revised by changing $\hbar\omega_v$ from 500 to 200 and to 833 cm^{-1}, respectively, with the first moments $S_u\hbar\omega_u$, $S_v\hbar\omega_v$ kept fixed. Despite the obvious 200 cm^{-1} phonons, the over-all band is poorly fitted with $\hbar\omega_v = 200$ cm^{-1}, and the chosen value $\hbar\omega_v = 500$ cm^{-1} gives the best fit. The corundum lattice has several vibration energies from 200 to 900 cm^{-1}.[2,13] The Cr^{+3} center evidently involves a number of these energies. The $\hbar\omega_u$, $\hbar\omega_v$ parameters in the SCC model must be regarded as average energies giving an over-all fit to band shapes disregarding fine structure.

McClure[2] shows the σ and π absorption bands to $^4T_2$ and $^4T_1$ at elevated temperatures. All bands shift to lower energy with increasing temperature. At the highest temperature, 1175 °K, the center of the $^4T_2$ σ band lies at 596 nm, its zero-phonon position at 2 °K. This 1175 °K band could not possibly be fitted with $h\nu_{zp,vu}$ at 596 nm. The lesson for the model is that the $^4T_2$ parabola must be shifted downward with increasing temperature. A $1.4kT$ shift matches McClure's measured shift, and this shift has been included in $h\nu_{zp,vu}$ cited above. This shift occurs for the $^4T_2$ and $^4T_1$ parabolas in both polarizations. Figure 1 shows these parabolas at 0 °K; at higher temperatures, they are lower.

McClure[2] explained the shift through thermal expansion of the lattice. Such shifts will occur for

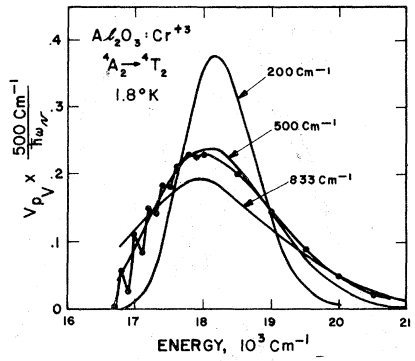

FIG. 2. Fit of the SCC model to the ruby σ absorption band to $^4T_2$ at 2 °K. The three computed bands for $\hbar\omega_v$ = 200, 500, and 833 cm^{-1} are multiplied by 500 cm^{-1}/$\hbar\omega_v$ so that the areas under these bands are the same.

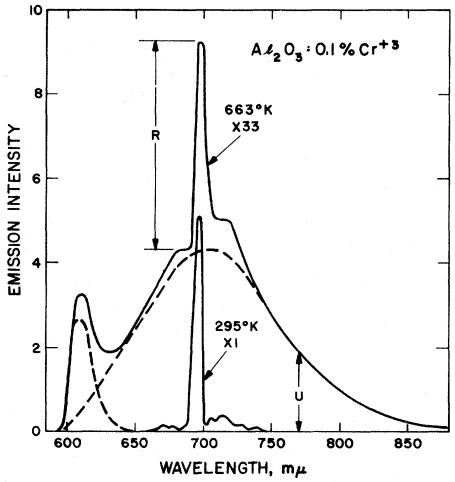

FIG. 3. Ruby emission spectrum showing the $^2E \rightarrow {}^4A_2$ narrow line and, at 663 °K, the $^4T_2 \rightarrow {}^4A_2$ broad band. The peak at 610 nm is due to filter overlap in the excitation and detection monochromators and should be ignored.

all FC-offset states, even large-offset states where the zero-phonon positions are known poorly. For example, Pohl's KBr F-center absorption bands discussed in the Huang-Rhys paper[14] show such a shift, and its magnitude is larger at $3.8kT$. This shift mimics the effect of the anharmonicites of the 10^{22} lattice modes and is another manifestation of multiple vibrational coordinates.

Figure 3 shows the emission band from $^4T_2$ together with the superimposed $^2E \rightarrow {}^4A_2$ narrow-line emission. Misu[4] and KM show similar emissions. At 295 °K where the $^4T_2$ population is small, one sees only the narrow-line and its modest phonon sidebands. At 663 °K, the narrow-line is 30 times smaller, and the emission is dominated by the $^4T_2 \rightarrow {}^4A_2$ band. The dashed curve estimates the division between the two emissions. The temperature shift of the narrow line is an order of magnitude smaller than the $1.4kT$ shift of the $^4T_2$ band, and ^2E-parabola downshift is neglected in the work here.

Figure 4 shows the model fit to the σ absorption bands to $^4T_2$ and $^4T_1$ and to the emission band from $^4T_2$ at high temperature. The curves with points are the experimental bands, absorption taken from McClure's 715 °K measurements,[2] emission from the 663 °K dashed curve in Fig. 3. The computed $^4A_2 \rightleftarrows {}^4T_2$ bands used the parameter values cited above and used to fit the 2 °K absorption band in Fig. 2. The fitted zero-phonon position $h\nu_{zp,vu}$ is 16 770 cm^{-1} at 2 °K, 16 125 cm^{-1} at 663 °K, and 16 075 cm^{-1} at 715 °K. Taking this shift into account, the absorption and emission bands are closer together and their asymmetry about $h\nu_{zp,vu}$ is smaller than envisioned in KM's paper. Indeed, the absorption and emission bands overlap, and the intensity of the emission band is decreased on its high-energy side due to self-absorption. No self-absorption correction was made to the fitted band in Fig. 4.

For the absorption to $^4T_1$, the fitted band used the $^4A_2(u)$, $^4T_1(v)$ parameters $\theta = 44°$, $a_{uv} = 5.230$, $\hbar\omega_v = 500$ cm^{-1}, $\hbar\omega_{zp,vu} = 21\,600$ $cm^{-1} - 1.4kT$. The offset is larger in this case, and the first moments are $S_v\hbar\omega_v = 3300$ cm^{-1} in absorption, $S_u\hbar\omega_u = 3790$ cm^{-1} in emission. Absorption is slightly stronger to $^4T_1$, and the V_{pV} values for $^4T_1$ were multiplied accordingly by 1.91 in Fig. 4.

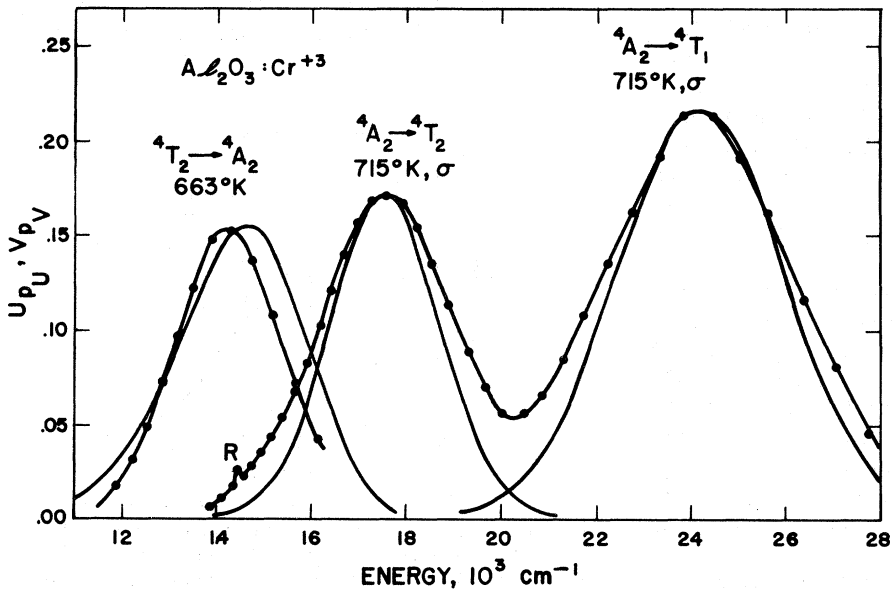

FIG. 4. Fit of the SCC model to the ruby $^4A_2 \rightarrow {}^4T_2$, $^4T_1$ absorption bands and the $^4T_2 \rightarrow {}^4A_2$ emission band at high temperature.

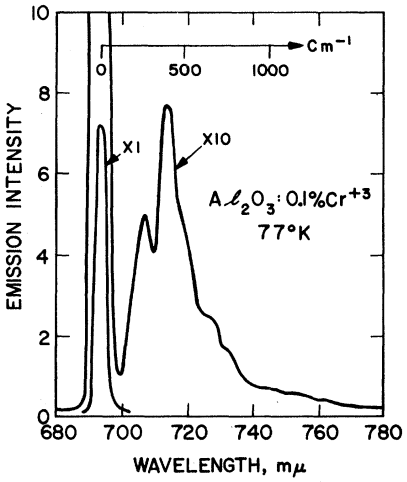

FIG. 5. Zero-phonon line and phonon sidebands of ruby $^2E \rightarrow {}^4A_2$ emission at 77°K.

C. Small-offset transitions

The small-offset states ^2E, $^2T_1$, $^2T_2$ are drawn with no offset in Fig. 1 for simplicity. Zero offset would exclude phonon sidebands or nonradiative transitions to $^4A_2$. The offsets can be estimated from the phonon sidebands. As one example, the $^2E \rightarrow {}^4A_2$ emission line and its phonon sidebands at 77 °K are shown in Fig. 5. Multiple phonon energies are again evident. The two most prominent are 280 and 430 cm^{-1}, and the 200 cm^{-1} phonon conspicuous in σ absorption to $^4T_2$ is not especially evident. Two-thirds of the emission is in the zero-phonon line (693.5 nm), and the first moment relative to this line is 160 cm^{-1}. Thus, our small-offset-case[1] description of $^4A_2(u) \rightleftarrows {}^2E(v)$ transitions adopts the parameters $\theta = 45°$, $a_{uv} = 1.265$, $\hbar\omega_0 = 400\ cm^{-1}$, and $h\nu_{zp,vu} = 14\,420\ cm^{-1}$. These values fix the Huang-Rhys-Pekar factor $S_0 = 0.4$, the first moments $S_0\hbar\omega_0 = 160\ cm^{-1}$, and the fraction of the emission in the zero-phonon line at low temperature $W_0 = \exp(-S_0) = 0.67$. The offsets of the $^2T_1$ and $^2T_2$ parabolas would be similar.

The first moments of the broad band to $^4T_2$ and the narrow line to ^2E differ by a factor of 10. However, the parabola offsets, proportional to a_{uv}, differ only by a factor of 3. Thus, in a properly drawn SCC diagram, the $^4T_2$ and ^2E offsets are not dramatically different. We lack sufficient information to draw all the offsets correctly. Nevertheless, the important ^2E, $^4A_2$ and $^4T_2$, $^4A_2$ offsets are known well, and rough estimates of the remaining offsets are good enough for the analysis of relaxation in this paper.

III. RELAXATION IN RUBY

A. Over-all description of relaxation

In the model, the nonradiative rate is $N_{uv}U_{p_U}$ for $v \rightarrow u$, $N_{vu}V_{p_V}$ for $u \rightarrow v$. Table I lists the computed nonradiative rates for all ruby downward transitions at 0 °K. At higher temperatures, the rates would be higher. The electronic factors N_{uv} or N_{vu} were always taken $10^{14}\ sec^{-1}$. The other model parameters are listed in the table; except as amended below, they are values used in Sec. II. for the optical bands. The computed rates range from 10^{13} to $10^{-27}\ sec^{-1}$. Thus, although the electronic factors were all taken $10^{14}\ sec^{-1}$ and some of the parameters were only estimated, the 40

TABLE I. Calculated nonradiative rates for all pairs of ruby downward transitions. The model parameters used to calculate these rates are also listed. These rates are for 0 °K and would be higher at higher temperatures.

Transition	θ	a_{uv}	$S_f\hbar\omega_f$ (cm^{-1})	$\hbar\omega_f$ (cm^{-1})	$h\nu_{zp,if}$ (cm^{-1})	$10^{14}\ U_{p_U}$ or $10^{14}\ V_{p_V}$ (sec^{-1})
$^4T_1 \rightarrow {}^2T_2$	44°	5.230	3790	536	610	8.4×10^{11}
$\rightarrow {}^4T_2\ \pi$	45°	1.297	350	833	4300	4.7×10^{9}
$\rightarrow {}^4T_2\ \sigma$	45°	1.297	350	833	4830	8.6×10^{8}
$\rightarrow {}^2T_1$	44°	5.230	3790	536	6640	2.4×10^{12}
$\rightarrow {}^2E$	44°	5.230	3790	536	7180	1.3×10^{12}
$\rightarrow {}^4A_2$	44°	4.051	3790	893	21600	2.7×10^{4}
$^2T_2 \rightarrow {}^4T_2\ \pi$	44°	3.526	1500	500	3690	1.3×10^{12}
$\rightarrow {}^4T_2\ \sigma$	44°	3.526	1500	500	4220	3.8×10^{11}
$\rightarrow {}^2T_1$	45°	0.849	161	893	6030	2.5×10^{5}
$\rightarrow {}^2E$	45°	0.849	161	893	6570	2.6×10^{4}
$\rightarrow {}^4A_2$	45°	0.849	161	893	20990	2.1×10^{-27}
$^4T_2\ \sigma \rightarrow {}^2T_1$	44°	3.526	1725	536	1810	2.0×10^{13}
$\rightarrow {}^2E$	44°	3.526	1725	536	2350	1.5×10^{13}
$\rightarrow {}^4A_2$	44°	2.731	1725	893	16770	2.3×10^{3}
$^2T_1 \rightarrow {}^2E$	45°	1.095	161	536	540	2.2×10^{13}
$\rightarrow {}^4A_2$	45°	0.849	161	893	14960	1.6×10^{-13}
$^2E \rightarrow {}^4A_2$	45°	0.849	161	893	14420	2.5×10^{-12}

orders of magnitude variation in the calculated rates insures that the model can make a first order analysis of relaxation. The competing emission rates are 1.4×10^2 sec^{-1} for the $^2E\rightarrow{}^4A_2$ narrow line and 2.3×10^4 sec^{-1} for the $^4T_2\rightarrow{}^4A_2$ broad band. Data fixing these emission rates will be shown below.

According to the rates in the table, excitation in $^4T_1$ goes to $^2T_2$, $^2T_1$, and ^2E by fast bottom crossovers, excitation in $^2T_2$ to $^4T_2$ similarly, and excitation in $^4T_2$ to $^2T_1$ and ^2E similarly. Excitation in $^2T_1$ goes to ^2E by fast small-offset multiphonon emission. From ^2E, small-offset multiphonon emission to $^4A_2$ is negligible, and excitation in ^2E either goes radiatively to $^4A_2$, or, if reexcited thermally to $^2T_1$ or $^4T_2$, goes radiatively from $^2T_1$ or $^4T_2$ to $^4A_2$ or nonradiatively from $^4T_2$ to $^4A_2$ via the $^4T_2$, $^4A_2$ outside crossover.

According to the listed rates, the risetime of ^2E emission under pulsed excitation should be $\sim10^{-13}$ sec for $^4T_2$ excitation and $\sim10^{-12}$ sec for $^4T_1$ excitation. Experiments have given only upper limits for these times. Pollack[15] found $<5\times10^{-9}$ sec for 300 °K $^4T_1$ excitation, and Everett[16] $<2\times10^{-9}$ sec for $^4T_2$ excitation at 2, 77, and 300 °K. In Everett's work, the absence of prompt $^4T_2\rightarrow{}^4A_2$ broad-band emission during the pulse gave an even shorter upper limit for the $^4T_2$ lifetime, namely, $<10^{-11}$ sec.

The zero-phonon energies $h\nu_{zp,if}$ in the table are known from absorption spectra. This energy divided by the final-state phonon energy $\hbar\omega_f$ gives the p_U or p_V number for which the nonradiative rate $N_{uv}U_{p_U}$ or $N_{vu}V_{p_V}$ is calculated. The weights U_{p_U} and V_{p_V} have integer indices. Since the ratios $h\nu_{zp,if}/\hbar\omega_f$ are not integers, we have followed the practice of interpolating U_{p_U} or V_{p_V} values logarithmically to noninteger $h\nu_{zp,if}/\hbar\omega_f$ indices.

The parabola phonon energies were taken 500 cm^{-1} for the large-offset $^4T_1$ and $^4T_2$ states and 536 cm^{-1} for the small-offset $^2T_2$, $^2T_1$, ^2E, and $^4A_2$ states, proportions required for $\theta=44°$. However, if a transition was slow ($<10^{10}$ sec^{-1}), the phonon energies were increased to 833 and 893 cm^{-1}. These larger energies give smaller p numbers and faster rates. The thinking is that, with multiple phonon energies actually present, larger-energy phonons would be emphasized in transitions releasing appreciable phonon energy.

B. Relaxation from $^4T_2$ and ^2E

For a detailed analysis of thermal quenching, we use the reduced three-state system $^2E(u)$, $^4T_2$ $\sigma(v)$, and $^4A_2(g)$. ^2E has 4 states and $^4T_2$ σ 8 states.[11] Inclusion of the $6\,^2T_1$ and $4\,^4T_2$ π states about 500 cm^{-1} above ^2E and $^4T_2$ σ, respectively, would not change the results significantly. The parameter values are taken as in Table I; in addition, the parabola downshifts are taken to be $1.4kT$ for $^4T_2$ σ and zero for ^2E. Thus, if $^2E(u)$ and $^4T_2$ $\sigma(v)$ are in thermal equilibrium, their population ratio is

$$\left.\frac{n_v}{n_u}\right|_T=\tfrac{8}{4}\,e^{-h\nu_{zp,vu}/kT}=2\,e^{1.4}\,e^{-2350\ \mathrm{cm}^{-1}/kT}, \tag{1}$$

where a factor $[1-\exp(-\hbar\omega_u/kT)]/[1-\exp(-\hbar\omega_v/kT)]$ near unity has been neglected.

The rate of the outside crossover $^4T_2\sigma(v)\rightarrow{}^4A_2(g)$ is $N_{gv}G_{p_G}$ where, from Table I, $N_{gv}=1\times10^{14}$ sec^{-1} and G_{p_G} is calculated for $\theta=44°$, $a_{gv}=2.731$, and $p_G=18.77$. This rate is of the order of 10^4 sec^{-1} and increases with temperature. The rate $N_{uv}U_{p_U}$ of the fast bottom crossover $^4T_2\sigma(v)\rightarrow{}^2E(u)$ is near 10^{13} sec^{-1}. This rate and the rate $N_{vu}V_{p_V}$ of the inverse $^2E\rightarrow{}^4T_2\sigma$ transition are not needed accurately. As stated earlier, the radiative rates are $R_{gu}=1.4\times10^2$ sec^{-1} for $^2E\rightarrow{}^4A_2$ and $R_{gv}=2.3\times10^4$ sec^{-1} for $^4T_2\sigma\rightarrow{}^4A_2$.

Excitation into v either feeds into u or goes radiatively or nonradiatively to g. Thus, the quantum efficiencies η_v, η_u of emission (total emission) for excitation into v and u, respectively, are related by

$$\eta_v=\frac{N_{uv}\,U_{p_U}\eta_u+R_{gv}}{N_{uv}\,U_{p_U}+R_{gv}+N_{gv}\,G_{p_G}}\ . \tag{2}$$

Since $N_{uv}\,U_{p_U}$ is $\sim10^{13}$ sec^{-1}, while R_{gv} and $N_{gv}\,G_{p_G}$ are $\sim10^4$ sec^{-1}, η_v and η_u differ only by $\sim10^{-9}$. Misu[4] and Morgenshtern and co-workers[17] have reported $\eta_u\approx1.0$, $\eta_v\approx0.7$ at room temperature. This 30% difference cannot be explained in the model. If the measurements are correct, some explanation not in the model is needed, e.g., ^2E and $^4T_2$ excitations might be absorbed in inequivalent sites.

For excitation at rates G_u into u and G_v into v, the equations for steady-state equilibrium are

$$\begin{aligned}&(R_{gu}+N_{vu}\,V_{p_V})\,n_u-N_{uv}\,U_{p_U}\,n_v=G_u\ ,\\ &-N_{vu}\,V_{p_V}\,n_u+(N_{uv}\,U_{p_U}+R_{gv}+N_{gv}\,G_{p_G})\,n_v=G_v.\end{aligned} \tag{3}$$

Thus, the population ratios for u and v excitation are

$$\begin{aligned}\left.\frac{n_v}{n_u}\right|_{G_u}&=\frac{N_{vu}V_{p_V}}{N_{uv}\,U_{p_U}+R_{gv}+N_{gv}\,G_{p_G}}\\ &\approx\frac{N_{vu}\,V_{p_V}}{N_{uv}\,U_{p_U}}=\left.\frac{n_v}{n_u}\right|_T,\\ \left.\frac{n_v}{n_u}\right|_{G_v}&=\frac{R_{gu}+N_{vu}\,V_{p_V}}{N_{uv}\,U_{p_U}}=\frac{R_{gu}}{N_{uv}\,U_{p_U}}+\left.\frac{n_v}{n_u}\right|_T,\end{aligned} \tag{4}$$

where $n_v/n_u|_T$ is the thermal-equilibrium ratio (1). The ratio $N_{vu}\,V_{p_V}/N_{uv}\,U_{p_U}$ is equal to $n_v/n_u|_T$ be-

cause $u \rightarrow v$ and $v \rightarrow u$ are inverse processes whose rates $N_{vu} V_{pV} n_u$, $N_{uv} U_{pU} n_v$ must be equal at thermal equilibrium.

Thus, for u excitation, u and v are always in thermal equilibrium and, for v excitation, are in thermal equilibrium above temperature T_c defined by $R_{gu}/N_{uv} U_{pU} = n_v/n_u|_T$, that is, by $kT_c = 2350\ \text{cm}^{-1}/2.30 \log_{10}(8.1 N_{uv} U_{pU}/R_{gu})$. T_c is 123 °K for the rates $N_{uv} U_{pU} = 1.5 \times 10^{13}\ \text{sec}^{-1}$, $R_{gu} = 1.4 \times 10^2\ \text{sec}^{-1}$ here. This estimate cannot be far from correct because a factor of 10 error in $N_{uv} U_{pU}$ would change T_c by only 10 deg.

For the system $u+v$, the total population n_{total}, the total radiative rate from the system W_{rad}, and the total rate from the system W_{total} are given by

$$\begin{aligned} n_{\text{total}} &= n_u + n_v, \\ W_{\text{rad}} &= R_{gu} n_u + R_{gv} n_v, \\ W_{\text{total}} &= W_{\text{rad}} + N_{gv} G_{pG} n_v. \end{aligned} \tag{5}$$

Above T_c, the ratio of $v \rightarrow g$ broad-band and $u \rightarrow g$ narrow-line emission is

$$\frac{R_{gv} n_v}{R_{gu} n_u}\bigg|_T = 164 \frac{n_v}{n_u}\bigg|_T = 1330\, e^{-2350\ \text{cm}^{-1}/kT}; \tag{6}$$

the quantum efficiency of the narrow-line emission is

$$\eta_{gu} \equiv \frac{R_{gu} n_u}{W_{\text{total}}} = \left[1 + \frac{R_{gv} n_v}{R_{gu} n_u}\bigg|_T \left(1 + \frac{N_{gv} G_{pG}}{R_{gv}}\right)\right]^{-1}; \tag{7}$$

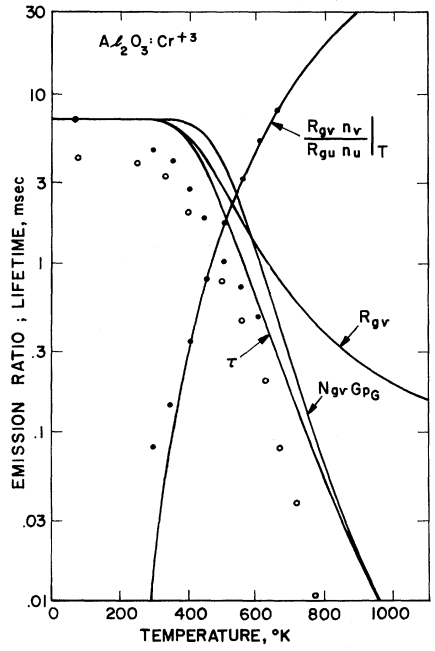

FIG. 6. Thermal buildup of the ruby broad-band to narrow-line emission ratio and thermal quenching of the ruby lifetime. The solid points were measured here, the open points by Kisliuk and Moore.

the quantum efficiency of the total emission is

$$\eta_{\text{total}} \equiv \frac{W_{\text{rad}}}{W_{\text{total}}} = \eta_{gu}\left(1 + \frac{R_{gv} n_v}{R_{gu} n_u}\bigg|_T\right); \tag{8}$$

and the lifetime of the u, v system is

$$\tau \equiv \frac{n_{\text{total}}}{W_{\text{total}}} = \frac{1}{R_{gu}} \eta_{gu}\left(1 + \frac{n_v}{n_u}\bigg|_T\right). \tag{9}$$

The total quantum efficiency is close to η_{gu} at low temperatures but is larger than η_{gu} at high temperatures where the broad-band $v \rightarrow g$ emission is important. The ratio $n_v/n_u|_T$ is only 0.3 at 1000 °K, so τ is proportional to η_{gu} to that temperature.

C. – Comparison with experiment

Measured and computed values of the broad-band to narrow-line emission ratio (6) are shown in Fig. 6. The measured ratios were taken from the amplitudes U at 770 nm and R at 594 nm shown in Fig. 3 and normalized to ratio 8 at 663 °K from the areas under the broad band and narrow line. The agreement between the measured and computed ratios confirms the 2350 cm^{-1} activation energy in (1) and (6) and determined our selection of the rate ratio $R_{gv}/R_{gu} = 164$. Analogous emission ratios are reported in Misu's[4] Fig. 4 (dotted curve). Although Misu describes these ratios by a 3000 cm^{-1} activation energy, they are better fitted by the 2350 cm^{-1} in (6).

Ruby lifetimes were measured with a 1-μsec flash lamp, excitation and detection monochromators, and a photon-counting system feeding a multichannel analyzer. Detections at 694 nm and at 770 nm (the narrow-line and broad-band emissions, respectively; see Fig. 3) yielded equal lifetimes, as befitting emissions from states in the same center in thermal equilibrium. Representative decays at a few temperatures are shown in Fig. 7. At the lower temperatures, the initial decay was slightly faster. Lifetimes were read from the later decay which was judged more representative of Cr^{+3} ions in dilute solution. These lifetimes, lifetimes from KM's Fig. 5, and lifetimes computed from (9) are shown in Fig. 6.

In the model, the lifetime quenches above 350 °K because of thermally activated ${}^4T_2\, \sigma(v) \rightarrow {}^4A_2\, (g)$ radiative and nonradiative transitions. The τ, R_{gv}, and $N_{gv} G_{pG}$ curves show τ quenchings computed for both processes and for the radiative and nonradiative processes taken separately. One sees that the initial quenching is due to the radiative process, but, above 600 °K, the quenching is dominated by the nonradiative process.

The measured lifetimes show a weak temperature dependence below 350 °K which cannot be explained by processes from ${}^4T_2$. Such processes would have to increase at least as fast as the ${}^4T_2$

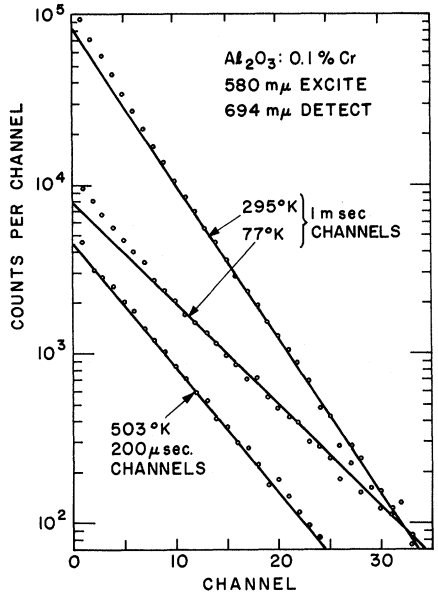

FIG. 7. Decays of ruby $^2E \rightarrow {}^4A_2$ line emission at a few temperatures. The straight lines fitted to the later stages of the decay correspond to lifetimes of 7.2 msec at 77°K, 4.7 msec at 295°K, and 1.02 msec at 503°K.

population n_v which increases by a factor 5 from 300 to 350 °K and faster at lower temperatures. The weak dependence must occur from ^2E. $^2E \rightarrow {}^4A_2$ nonradiative transitions are negligible in the model here, $\sim 10^{-9}$ sec^{-1} at 1200 °K. Thus, the weak dependence must be due to a non-Condon term in the $^2E \rightarrow {}^4A_2$ radiative rate or to interactions from ^2E with other impurity centers.

KM found the activation energy describing the initial lifetime quenching above 350 °K to be 1200 cm^{-1} rather than the expected 2350 cm^{-1}. Their analysis did not include the $\frac{8}{4}$ weight ratio and the $1.4kT$ parabola downshift in (1) and (6). With these factors included, their estimate for the activation energy would have been closer to 2350 cm^{-1}.

In reviewing the ruby work, Forster[8] was persuaded by the different measured quantum efficiencies for ^2E and $^4T_2$ excitation[4,17] and by KM's factor-of-2 activation-energy discrepancy to disallow KM's sequence of ruby temperature effects. Instead, he advanced a model in which ^2E and $^4T_2$, under $^4T_2$ excitation, do not come into thermal equilibrium until 500 °K. Forster's view is summarized succinctly on the last page of Ref. 18. KM's activation-energy discrepancy is largely resolved here; and, as discussed above in connection with (2), different quantum efficiencies for ^2E and $^4T_2$ excitation cannot be explained by the SCC model. Forster's interpretation is not possible because, as discussed in connection with (4), ^2E and $^4T_2$ come into thermal equilibrium near 123 °K.

Figure 8 shows measured and computed values of the total quantum efficiency (8). Values from KM's Fig. 5 are included. In the model, η_{total} quenches above 450 °K because of thermally activated $^4T_2 \rightarrow {}^4A_2$ crossovers. One of the reasons for taking the $^4T_2$ parabola flatter than the $^4A_2$ parabola as described by $\theta = 44°$ and the parabola phonon energies $\hbar\omega_v$, $\hbar\omega_t$ large near 800 cm^{-1} was to obtain the agreement shown here between measured and computed efficiencies. If θ were held at 44° but $\hbar\omega_v$ were decreased from 833 to 500 cm^{-1}, the model gives the quenching shown by the 500-cm^{-1} curve. Similarly, if the phonon energies were held near 800 cm^{-1} but θ were increased from 44° to 44.5° (force constants more equal), the model gives the 44.5° quenching curve. Either of these alternatives gives the quenching at too high temperature.

The $^4T_1$ curve shows the predicted quenching if the losses are taken not through $^4T_2$ but through the higher but larger-offset state $^4T_1$. This curve was calculated from the $^4T_1$, $^4A_2$ parameters in Table I and a $1.4kT$ $^4T_1$ parabola downshift. Despite the larger offset, the $^4T_1$ population is just too low, and the quenching occurs at too high temperature.

KM analyzed nonradiative losses using Kiel's multiphonon-emission rate $A_K \epsilon^p [1 + \langle m \rangle_v]^p$.[7] This formula is applicable to small-offset transitions such as $^2E \rightarrow {}^4A_2$ but is inaccurate for the large-offset $^4T_2 \rightarrow {}^4A_2$ crossover.[1] Comparing the observed temperature quenching with Kiel's $[1 + \langle m \rangle_v]^p$ temperature dependence, KM concluded that $^4T_2 \rightarrow {}^4A_2$ uses small-energy phonons ≤ 500 cm^{-1} (large p number). Their comparison neglected the absolute magnitude of the rate. As discussed above, the QMSCC model requires large-energy

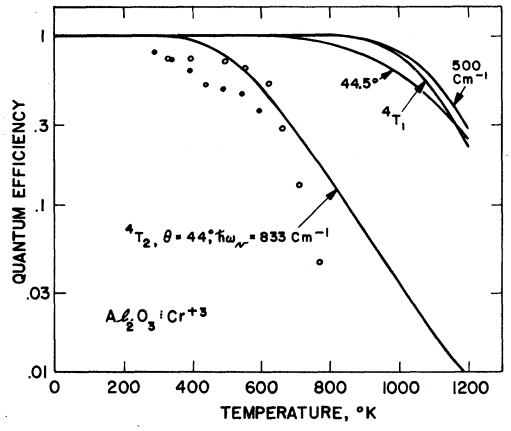

FIG. 8. Thermal quenching of ruby total emission. The solid points were measured here, the open points by Kisliuk and Moore.

TABLE II. Breakdown of the ruby $^4T_2\,\sigma(v) \rightarrow {}^4A_2(g)$ nonradiative transition into individual $v_m \rightarrow g$ rates. The parameter values are $\theta = 44°$, $a_{gv} = 2.731$, $\hbar\omega_g = 893$ cm^{-1}, $p_G = 19$, $N_{gv} = 1\times10^{14}$ sec^{-1}.

m	$G^2_{19,m}$	$N_{gv}(1-r_v)r_v^m G^2_{19,m}$, sec^{-1} 499 °K	666 °K	856 °K
0	1.51×10^{-11}	1370	1260	1140
1	3.14×10^{-10}	2590	4330	5830
2	3.10×10^{-9}	2320	7070	14210
3	2.02×10^{-8}	1370	7620	22840
4	9.95×10^{-8}	613	6200	27720
5	3.98×10^{-7}	222	4100	27350
6	1.36×10^{-6}	69	2310	22960
7	4.04×10^{-6}	19	1140	16890
8	1.08×10^{-5}	5	503	11150
9	2.64×10^{-5}	1	203	6700
10	5.93×10^{-5}		75	3720
11	1.24×10^{-4}		26	1920
12	2.45×10^{-4}		9	933
13	4.56×10^{-4}		3	428
14	8.06×10^{-4}		1	187
15	1.38×10^{-3}			79
16	2.35×10^{-3}			33
17	3.79×10^{-3}			13
18	5.80×10^{-3}			5
	$N_{gv}G_{19}$	8580	34840	164100
	$\langle m\rangle_{19}$	1.81	3.31	5.09
	$\langle m\rangle_v$	0.100	0.198	0.327
	$E_{19}/\hbar\omega_v$	1.71	3.11	4.76
	A_{19}/N_{gv}	5.2×10^{-9}	9.5×10^{-8}	13.0×10^{-7}
	$\hbar\omega_v/kT$	2.4	1.8	1.4
	r_v	0.0907	0.1653	0.2466

phonons near 800 cm^{-1} (smaller p number) to explain the quenching.

The measured quantum efficiencies were only relative values and were normalized to 0.8 at 295 °K. Their temperature dependence near room temperature is consistent with measured absolute quantum efficiencies less than unity at room temperature.[4,17,19] The weak temperature dependence of η_{total} below 450 °K cannot be due to processes from $^4T_2$ which would increase at least as fast as the $^4T_2$ population n_v. It must be due either to changes in the $^4A_2 \rightarrow {}^4T_2$ excitation rate with temperature which were not taken into account or to losses from ^2E. The $^2E \rightarrow {}^4A_2$ nonradiative transitions are negligible in the model, and any losses from ^2E must be attributed to interactions with other impurity ions.

D. Detailed picture of the $^4T_2 \rightarrow {}^4A_2$ crossover

As discussed in Ref. 1, the U, V-matrix method gives the breakdown of the nonradiative rates from the individual initial vibrational states. Table II, similar to the tables in Ref. 1, shows this breakdown for the $^4T_2\,\sigma(v) \rightarrow {}^4A_2(g)$ outside crossover. The first column gives the effective FC factors $G^2_{p_G m}$ from the initial vibrational states v_m, the remaining columns the corresponding thermal-FC weights $(1-r_v)\,r_v^m\,G^2_{p_G m}$ at a few temperatures. The summed thermal-FC weights multiplied by the electronic factor N_{gv} is the total nonradiative rate $N_{gv}G_{p_G}$. These values were computed for the $^4T_2\,\sigma$, $^4A_2$ parameters in Table I except that here $p_G = 19$; in Table I and Figs. 6 and 8, the total rate was interpolated logarithmically to $p_G = 18.77$. The total rate increases with temperature and passes the $^4T_2 \rightarrow {}^4A_2$ radiative rate $R_{gv} = 2.3\times10^4$ sec^{-1} by the middle temperature shown, 666 °K.

The v, g crossover (see Fig. 1) lies about 19000 cm^{-1} above the $^4T_2\,\sigma(v)$ parabola minimum near the v_m vibrational level $m = 22$. Thus, the thermal-FC weights in the table show the transitions taking place at m levels closer to the v-parabola minimum than to the v, g crossover. The mean m level of the transitions is $\langle m\rangle_{p_G} = 1.8$, 3.3, and 5.1 at the three temperatures shown. Thus, Mott's crossover rate[6] $A_M \exp(-E_X/kT)$ poorly describes such a transition.[1]

As discussed in Ref. 1, if a single-activation-energy expression $A_{p_G}\exp(-E_{p_G}/kT)$ is fitted to the nonradiative rate $N_{gv}G_{p_G}$ at any temperature T, the activation energy E_{p_G} is approximately the mean level $\langle m\rangle_{p_G}\hbar\omega_v$ of the transitions, and the rate A_{p_G} is of the order of the electronic factor N_{gv} times the FC factor $G^2_{p_G m}$ for m taken at the mean level $m = \langle m\rangle_{p_G}$ of the transitions. The values in the lower rows of the table illustrate these relationships numerically.

IV. EMERALD

As compared with ruby, the $^4T_2$ parabola of emerald is about 2000 cm^{-1} lower and has somewhat less FC offset. $^4T_2 \rightleftarrows {}^4A_2$ transitions are not much changed thereby, but the energy activation from ^2E to $^4T_2$ is substantially reduced. Thus, the $^4T_2$ population and the $^4T_2 \rightarrow {}^4A_2$ broad-band emissions build up at much lower temperatures. Losses through the $^4T_2 \rightarrow {}^4A_2$ outside crossover occur as in ruby above 450 °K.

The model will be fitted to emerald absorption data due to Wood[20] and emission and quenching data due to KM.[5] For the $^2E(u) \rightarrow {}^4A_2(g)$ narrow-line emission, the parameter values are $h\nu_{zp,ug} = 14650$ cm^{-1} and $R_{gu} = 7\times10^2$ sec^{-1}. For the $^4T_2 \rightleftarrows {}^4A_2$ broad bands, the 4 $^4T_2$ states seen for the π polarization are lower than the 8 $^4T_2$ states seen for the σ polarization.[20] For the $^4T_2\,\pi(v) \rightleftarrows {}^4A_2(g)$ broad bands, the parameters are $\theta = 44°$, $a_{gv} = 3.054$, $\hbar\omega_v = 500$ cm^{-1}, $h\nu_{zp,vg} = 15150$ cm$^{-1} - 2.1kT$, and $R_{gv} = 3\times10^4$ sec^{-1}. These values fix $\hbar\omega_g = 536$ cm^{-1}, $S_v = 2.25$, $S_g = 2.413$, and the first moments $S_v\hbar\omega_v = 1125$ cm^{-1} in absorption, $S_g\hbar\omega_g = 1294$ cm^{-1} in emission. For the $^4T_2\,\pi(v) \rightarrow {}^4A_2(g)$ outside crossover emphasizing larger-energy phonons, we increase $\hbar\omega_v$ to 750 cm^{-1} with θ and the first moments fixed, and N_{gv} is taken 1×10^{14} sec^{-1}. These

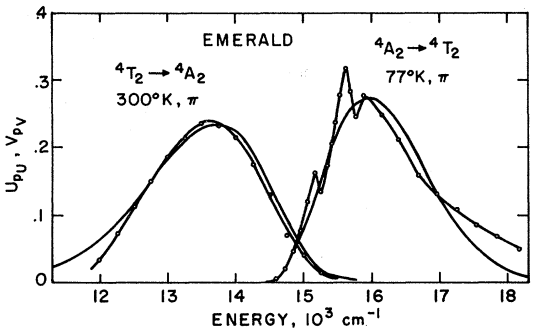

FIG. 9. Fit of the SCC model to the emerald $^4A_2 \rightleftarrows {}^4T_2$ absorption and emission bands.

choices decrease a_{gv} to 2.493 and give a cross-over rate $N_{gv} G_{p_G}$ with $p_G = 18.84$.

For these values, Eqs. (1) and (6) for the $^4T_2\pi/{}^2E$ population ratio and the $^4T_2\pi \rightarrow {}^4A_2/{}^2E \rightarrow {}^4A_2$ emission ratio become, for emerald,

$$\left.\frac{n_v}{n_u}\right|_T = \frac{4}{4} e^{-\hbar\omega_{gp,vu}/kT} = e^{2.1} e^{-500\ \mathrm{cm}^{-1}/kT}\ , \qquad \left.\frac{R_{gv} n_v}{R_{gu} n_u}\right|_T = 43 \left.\frac{n_v}{n_u}\right|_T = 352\, e^{-500\ \mathrm{cm}^{-1}/kT}\ , \tag{10}$$

respectively. Otherwise, Eqs. (1)–(9) remain valid for emerald. The downshifted $^4T_2\pi$ parabola passes below the ^2E parabola at $2.1kT = 500$ cm^{-1}, or $T = 343$ °K. The estimate beneath Eq. (4) for the temperature T_c above which ^2E and $^4T_2$ are in thermal equilibrium for $^4T_2$ excitation is, for emerald, $T_c = 28$ °K.

Figure 9 compares the calculated $^4A_2 \rightleftarrows {}^4T_2\pi$ optical bands with Wood's 77 °K absorption band and KM's 300 °K emission band. In the model, the downshifted zero-phonon position $h\nu_{gp,vg}$ lies at 15 040 cm^{-1} at 77 °K and 14 710 cm^{-1} at 300 °K. The $^2E \rightleftarrows {}^4A_2$ narrow line, not shown in the figure, lies at 14 650 cm^{-1}. The observed peak at 15 140 cm^{-1} may be the $^4A_2 \rightarrow {}^2T_1$ absorption line. Otherwise, as in the ruby case, the model does not address phonon structure on the low-energy side of the absorption band. The over-all band shapes are fairly well fitted by the assumed parameter values.

Figure 10 compares quenching data from KM's Fig. 1 with η_{total} and τ calculated from Eqs. (8) and (9). The lifetime τ quenches because of thermally activated radiative and nonradiative $^4T_2\pi \rightarrow {}^4A_2$ transitions, the efficiency η_{total} because of the nonradiative transitions alone. The portion of the τ quenching due to the radiative transitions alone is shown by the R_{gv} curve. As contrasted with ruby, the radiative and nonradiative quenchings are well separated in temperature here. This feature enabled KM to develop the sequence of temperature effects. As cited above, the $^4T_2\pi \rightarrow {}^4A_2$ nonradiative rate was fitted with the high phonon energy $\hbar\omega_v = 750$ cm^{-1}. As in ruby, these nonradiative transitions occur at levels well below the $^4T_2$, $^4A_2$ crossover.

The emerald quenchings in Fig. 10 can be fitted not as well but fairly well with $n_v/n_u|_T = \exp(-388\ \mathrm{cm}^{-1}/kT)$ and $R_{gv} = 8.5 \times 10^4$ sec^{-1}, that is, with no $^4T_2$ parabola downshift and the $^4T_2 \rightarrow {}^4A_2$ radiative rate increased a factor of 3. Thus, the R_{gv} rate deduced by fitting the data is sensitive to the amount of parabola downshift used.

V. CONCLUSIONS

Radiative and nonradiative transitions in ruby and emerald are analyzed according to the QMSCC model. The energy parabolas are positioned so that the thermal-FC weights account consistently for the optical bands and for the temperature quenchings of emissions. Even though many vibrational coordinates are present, the thermal-FC weights in the single coordinate allow a first-order quantitative description of relaxation. The parabola phonon energies $\hbar\omega_u$, $\hbar\omega_v$ are average energies. Energies near 500 cm^{-1} account for the over-all optical-band shapes disregarding fine structure, and energies near 800 cm^{-1} account for nonradiative transitions releasing a large phonon energy.

Lattice thermal expansion lowers the larger-offset parabolas a few kT units. Allowing for this effect, the first moments and asymmetry of the $^4T_2 \rightarrow {}^4A_2$ optical bands about their zero-phonon position are smaller than envisioned previously. The moments are 1500 cm^{-1} in absorption and 1725 cm^{-1} in emission for ruby; 1125 and 1300 cm^{-1} for emerald. The thermal lowering of the $^4T_2$ parabola enhances $^4T_2$ thermal repopulation from ^2E and, therefore, $^4T_2 \rightarrow {}^4A_2$ radiative and nonradiative transitions.

In the model, excitation relaxes very quickly and efficiently to ^2E, nonradiative $^2E \rightarrow {}^4A_2$ transitions

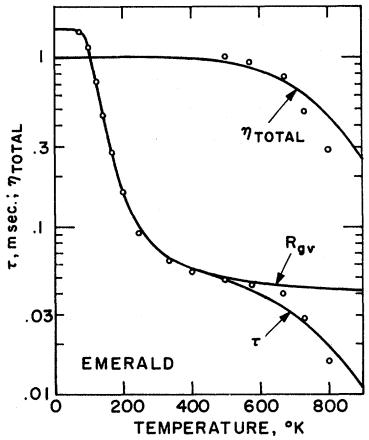

FIG. 10. Thermal quenching of emerald lifetime and total emission.

are negligible, and emission is divided between $^2E \rightarrow {}^4A_2$ narrow-line emission and thermally activated $^4T_2 \rightarrow {}^4A_2$ broad-band emission. As the faster broad-band emission builds up, the lifetime quenches–above 350 °K in ruby, 100 °K in emerald. The deduced broad-band emission rates are 2.3×10^4 sec^{-1} for ruby, 3×10^4 sec^{-1} for emerald. Above 450 °K in both materials, $^4T_2 \rightarrow {}^4A_2$ nonradiative transitions become important and cause a further quenching of the lifetime and a quenching of total quantum efficiency.

Different quantum efficiencies for ^2E and $^4T_2$ excitation are not possible in the model. Weak temperature dependences of efficiency below 450 °K must be attributed to changes of the $^4A_2 \rightarrow {}^4T_2$ excitation rate with temperature which were not taken into account or to interactions from ^2E with other impurity centers. For ruby, weak temperature dependences of the lifetime below 350 °K must be attributed to a non-Condon term in the $^2E \rightarrow {}^4A_2$ radiative rate or to interactions from ^2E with other impurity ions.

---

[1]C. W. Struck and W. H. Fonger, J. Lumines. 11, 1 (1975).

[2]D. S. McClure, J. Chem. Phys. 36, 2757 (1962).

[3]D. S. McClure, in *Solid State Physics*, edited by F. Seitz and D. Turnbull (Academic, New York, 1959), Vol. 9, p. 399.

[4]A. Misu, J. Phys. Soc. Jpn. 19, 2260 (1964).

[5]P. Kisliuk and C. A. Moore, Phys. Rev. 160, 307 (1967).

[6]N. F. Mott, Proc. R. Soc. Lond. A 167, 384 (1938); R. W. Gurney and N. F. Mott, Trans. Faraday Soc. 35, 69 (1939).

[7]H. W. Moos, J. Lumines. 1, 2, 106 (1970); A. Kiel, in *Proceedings of the Third International Conference on Quantum Electronics, Paris*, 1963, edited by P. Grivet and N. Bloembergen (Columbia U.P., New York, 1964), p. 765.

[8]L. S. Forster, in *Transition Metal Chemistry*, edited by R. L. Carlin (Marcel Dekker, New York, 1969), Vol. 5, p. 25.

[9]C. Manneback, Physica (Utr.) 17, 1001 (1951); W. H. Fonger and C. W. Struck, J. Chem. Phys. 60, 1994 (1974).

[10]Kisliuk and Moore, Ref. 5, inadvertently described $^4A_2$ as flatter than $^4T_2$. However, they meant the situation described here.

[11]J. Brossel and J. Margerie, in *Paramagnetic Resonance*, edited by W. Low (Academic, New York, 1963), Vol. II, p. 535.

[12]B. N. Grechushnikov and P. P. Feofilov, Zh. Eksp. Teor. Fiz. 29, 384 (1955) [Sov. Phys.-JETP 2, 330 (1955)].

[13]R. S. Krishnan, Proc. Ind. Acad. Sci. A 26, 450 (1947).

[14]K. Huang and A. Rhys, Proc. R. Soc. Lond. A 204, 406 (1950).

[15]S. A. Pollack, J. Appl. Phys. 38, 13 (1967).

[16]P. N. Everett, J. Appl. Phys. 41, 3193 (1970).

[17]E. E. Bukke and Z. L. Morgenshtern, Opt. Spektrosk. 14, 687 (1963) [Opt. Spectrosc. 14, 362 (1963)]; Z. L. Morgenshtern and V. B. Neustruev, in *Luminescence of Crystals, Molecules, and Solutions*, edited by F. Williams (Plenum, New York, 1973), p. 524.

[18]F. D. Camassei and L. S. Forster, J. Chem. Phys. 50, 2603 (1969).

[19]F. Castelli and L. S. Forster, J. Lumines. 8, 252 (1974).

[20]D. L. Wood, J. Chem. Phys. 42, 3404 (1965).